Polarization and far-field diffraction patterns of total internal reflection corner cubes

T. W. Murphy, Jr.[1,*] and S. D. Goodrow[1]

[1]*Center for Astrophysics and Space Sciences, University of California, San Diego, 9500 Gilman Drive, MC-0424, La Jolla, CA 92093-0424, USA*

*Corresponding author: `tmurphy@physics.ucsd.edu`

Many corner cube prisms, or retroreflectors, employ total internal reflection (TIR) via uncoated rear surfaces. The different elliptical polarization states emerging from the six unique paths through the corner cube complicate the far-field diffraction pattern by introducing various phase delays between the six paths. In this paper, we present a computational framework to evaluate polarization through TIR corner cubes for arbitrary incidence angles and input polarization states, presenting example output for key normal-incidence conditions. We also describe a method to produce far-field diffraction patterns resulting from the polarization analysis, presenting representative images—broken into orthogonal polarizations, and characterizing key cases. Laboratory confirmation is also presented for both polarization states and far-field diffraction patterns.

1. Introduction

Solid glass corner cube prisms (or, more generally, corner cube retroreflectors or CCRs) are used in interferometers, surveying references, gravimeters, and for laser ranging to satellites and the Moon. CCRs may either have a metallic reflective coating on the rear surface, such as silver or aluminum, or be uncoated to operate via total internal reflection (TIR). Within 17° of normal-incidence, TIR CCRs reflect 100% of the incident light at any azimuthal angle, ignoring reflection losses at the front surface (which may be anti-reflection coated). Comparatively, silver coatings operating at 96% will lose 12% of the flux due to three rear surface reflections, and aluminum coatings at 91% will sacrifice 25% of the light. For some

applications, absorption of incident light (e.g., sunlight) by the reflective coating results in strong thermal gradients within the prism, in turn leading to phase distortions that disturb the far-field diffraction pattern. In these cases, TIR cubes are preferred.

On the other hand, coated corner cubes have little effect on the input polarization state, so that in the absence of thermal gradients or other distorting influences, the far-field diffraction pattern from such a corner cube will approach that of a perfect Airy pattern corresponding to the circular aperture of the corner cube. TIR corner cubes, by contrast, generally introduce elliptical polarization at each reflection. Each of the six surface sequence permutations will in general produce a different output polarization, corresponding to phase offsets between the six paths. The resulting far-field diffraction pattern for a fused silica CCR has a central intensity only 26% that of the perfect reflector case. Only 36.1% of the total flux falls within a radius of $1.22\lambda/D$—corresponding to the first null in the Airy pattern—where λ is the wavelength and D is the diameter of the corner cube aperture. The comparable measure for the Airy function is 83.8%.

The literature contains a number of papers describing polarization and diffraction of TIR CCRs, but some are inconsistent with each other, and none of them provide an adequate framework for a comprehensive assessment of CCR performance compatible with our goals. Specifically, Peck (1962) [1] finds polarization eigenmodes for TIR CCRs at normal incidence—primarily with an interest in using CCRs in optical cavities. Liu and Azzam (1995) [2] offer a comprehensive treatment of the polarization states emerging from TIR CCRs, along with laboratory measurements of Stokes parameters. The focus follows that of Peck: calculating eigenmodes in a coordinate system that has a reflection relative to the input coordinates. Hodgson and Chipman (1990) [3] also present laboratory data along with a mathematical development, but we find the results to be incompatible with ours and other works—as if the solid cube under examination employed reflective coatings rather than TIR. Scholl (1995) [4] performs raytrace analysis to track the state of the electric field within imperfect corner cubes, but does not treat TIR explicitly. Chang et al. (1971) [5] provide an impressive analytic calculation of the far-field diffraction pattern of a TIR CCR at normal incidence and linear input polarization, along with some useful quantitative handles. This paper also separates the diffraction patterns into orthogonal polarization states and provides laboratory checks on the results, which prompted us to use this paper as a useful standard against which to compare our normal-incidence linear polarization results. In a related vein, Arnold produced a series of special reports on methods for calculating CCR transfer functions [6]. Most recently, Sadovnikov and Sokolov (2009) [7], and later Sokolov and Murashkin (2011) [8], contribute a work most similar to our own, presenting diagrams of polarization and diffraction patterns at different input polarizations for the normal incidence case. However, the works were not readily adaptable to our needs because: 1) coordinate systems and

plotting conventions are not clearly described; 2) the corner cubes considered do not appear to be circularly cut; and 3) the presentation is not geared toward instructing readers on how to develop their own analysis capability—as this work aims to do.

Our ultimate goal is to assess the far-field diffraction pattern from TIR CCRs subject to thermal gradients for application in our lunar laser ranging project [9] (see the companion paper on thermal gradients within CCRs [10]). Because the target CCR is in relative tangential motion with respect to the line of sight, velocity aberration shifts the pattern relative to our receiving telescope. We therefore sample the shoulder of the central diffraction peak, and thus are not content with knowledge of the central irradiance of the diffraction pattern. Even though the lunar CCRs are designed to minimize thermal gradients, we observe strong evidence that thermal gradients are developing at certain lunar phases—likely due to solar illumination of dust deposited on the front faces of the prisms [11]. We have found the existing literature to be insufficient for prescribing analysis algorithms that we might emulate, and further found inadequate published experimental results against which to verify our results.

We describe here a technique to analyze corner cube polarization and diffraction patterns at arbitrary angles of incidence that should be straightforward to program into a computer language (we used Python, and make our code available online). Moreover, we display graphical output of polarization states and of diffraction patterns that should be useful for comparison and as a demonstration of the general behavior of TIR CCR diffraction. Laboratory polarization measurements confirm the analysis, and far-field diffraction patterns verify the final result.

2. Corner Cube Geometry and Raytracing

Figure 1 depicts the geometry and orientation of a circularly cut CCR within a global right-handed Cartesian coordinate system. Rear faces are labeled A, B, and C, so that a particular ray path through the CCR can be labeled as ACB, for instance.

The three normal vectors for the rear surfaces form an orthonormal set:

$$\hat{\mathbf{n}}_A = \tfrac{1}{\sqrt{6}} \begin{pmatrix} -1 \\ -\sqrt{3} \\ \sqrt{2} \end{pmatrix}$$

$$\hat{\mathbf{n}}_B = \tfrac{1}{\sqrt{6}} \begin{pmatrix} 2 \\ 0 \\ \sqrt{2} \end{pmatrix} \quad . \tag{1}$$

$$\hat{\mathbf{n}}_C = \tfrac{1}{\sqrt{6}} \begin{pmatrix} -1 \\ \sqrt{3} \\ \sqrt{2} \end{pmatrix}$$

We define the distant observer's angular position relative to the CCR by an azimuth, A—
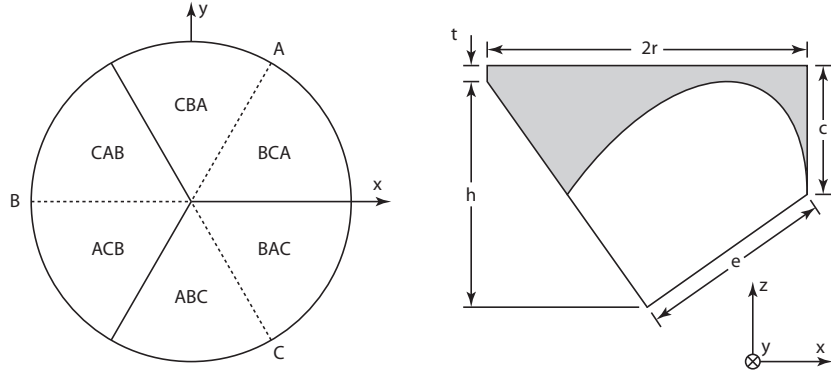
Fig. 1. Corner cube geometry and global coordinate system. The three back faces are labeled A, B, and C. Dotted lines represent reflections of the real edges. Three-letter sequences placed on each "wedge" identify the exit location for the six unique paths through the CCR (the corresponding input wedge is diametrically opposite). The view at right is along the global y-axis, with face C exposed to view. In units of the circular radius, r, $h = \sqrt{2}$, $e = \sqrt{\frac{3}{2}}$, and $c = \sqrt{\frac{1}{2}}$. The distance t is arbitrary, representing the height of the uninterrupted cylinder around the CCR.

measured from the x–axis and increasing toward the y–axis—and an inclination, i—away from the z–axis, so that $\hat{\mathbf{k}}_0 = \langle -\sin i \cos A, \ -\sin i \sin A, \ -\cos i \rangle$. Snell's law can be applied at the CCR front face to redirect an incident light ray into a new $\hat{\mathbf{k}}$, while reflection within the CCR changes the ray direction according to $\hat{\mathbf{k}} \rightarrow \hat{\mathbf{k}} - 2(\hat{\mathbf{k}} \cdot \hat{\mathbf{n}})\hat{\mathbf{n}}$, where $\hat{\mathbf{n}}$ is the surface normal in question.

We define a frame for input polarization that we associate with horizontal ($\hat{\mathbf{s}}_0$) and vertical ($\hat{\mathbf{p}}_0$) in such a way that the horizontal unit vector is perpendicular to both $\hat{\mathbf{k}}_0$ and $\hat{\mathbf{z}}$, which itself is the front surface normal. Explicitly,

$$
\begin{aligned}
\hat{\mathbf{s}}_0 &= \langle -\sin A, \ \cos A, \ 0 \rangle \\
\hat{\mathbf{p}}_0 &= \hat{\mathbf{s}}_0 \times \hat{\mathbf{k}}_0
\end{aligned}
\quad , \tag{2}
$$

where A, again, is the azimuth of the observer. We will present both input and output polarization states in the globally-referenced observer frame of Eq. 2, which will ultimately require a coordinate flip owing to the retroreflection.

On approach to each interface one must transform into the local s and p coordinate system corresponding to directions perpendicular and parallel to the plane of incidence, respectively. The s–p frame is described by

$$
\begin{aligned}
\hat{\mathbf{s}} &= \frac{\hat{\mathbf{k}} \times \hat{\mathbf{n}}}{|\hat{\mathbf{k}} \times \hat{\mathbf{n}}|} \\
\hat{\mathbf{p}} &= \hat{\mathbf{s}} \times \hat{\mathbf{k}}
\end{aligned}
\quad , \tag{3}
$$

which happens to be aligned with the global x–y frame for light approaching the corner cube from azimuth $A = -90°$, and appearing right-handed if looking along $\hat{\mathbf{k}}$. The transformation between some arbitrary u–v frame perpendicular to the propagation direction and the s–p frame for the upcoming surface interface can be determined from the four-quadrant arctangent

$$
\alpha = \text{atan2}(\hat{\mathbf{s}} \cdot \hat{\mathbf{v}}, \hat{\mathbf{s}} \cdot \hat{\mathbf{u}}), \tag{4}
$$

as depicted in Figure 2. After the interface—whether refractive or reflective—the propagation direction, $\hat{\mathbf{k}}$, is altered by some rotation about the $\hat{\mathbf{s}}$ direction. Consequently, $\hat{\mathbf{s}}$ is unchanged at a single interface, while $\hat{\mathbf{p}}$ must be re-evaluated according to Eq. 3. As one steps through the corner cube, the $\hat{\mathbf{s}}$ and $\hat{\mathbf{p}}$ vectors become the $\hat{\mathbf{u}}$ and $\hat{\mathbf{v}}$ vectors for the next application of Eq. 4.

For reference, the rotation angles, α, for all six path sequences through the corner cube at normal incidence are given in Table 1, where the initial u–v coordinate system is aligned to the global x–y frame ($A = -90°$). The last rotation, α_4, aligns the final $\hat{\mathbf{p}}$ vector with $\hat{\mathbf{p}}_0$, while the retroreflection ($\hat{\mathbf{k}} \rightarrow -\hat{\mathbf{k}}_0$) results in a coordinate flip so that $\hat{\mathbf{s}}$ points along $-\hat{\mathbf{s}}_0$.
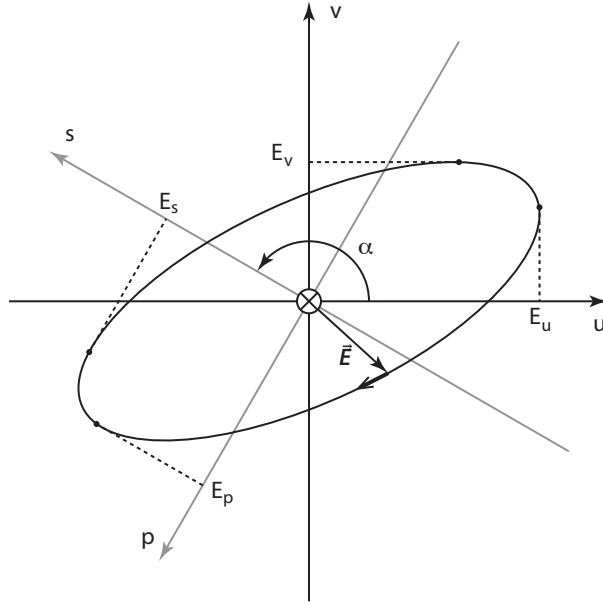
Fig. 2. Coordinate system for representation of elliptical polarization, looking along the propagation direction (note central × denoting $\hat{\mathbf{k}}$ going into the page). By the conventional definition, the electric field vector pictured rotates in a left-handed sense, when looking toward the light source.

Table 1. Rotation Sequences, in Degrees

path	α_1	α_2	α_3	α_4
ACB	150	−60	60	−90
ABC	150	60	−60	30
BAC	−90	−60	60	30
BCA	−90	60	−60	150
CBA	30	−60	60	150
CAB	30	60	−60	−90

3. Polarization and Phases

We describe the electric field transverse to the direction of propagation by a two-component vector in an orthogonal basis, expressed in the global 3-D coordinate system by the unit vectors $\hat{\mathbf{u}}$ and $\hat{\mathbf{v}}$. Because pathlengths within a perfect CCR are independent of position for a given $\hat{\mathbf{k}}_0$, we can suppress the phase advance associated with forward propagation, concentrating only on the temporal and static phase offsets—the latter changing only at interfaces. In the generalized coordinates, u and v, the electric field vector follows

$$\vec{E} = \begin{pmatrix} E_u \cos(\omega t + \delta_u) \\ E_v \cos(\omega t + \delta_v) \end{pmatrix}, \tag{5}$$

where E_u and E_v are positive electric field amplitudes in the u and v directions and δ_u and δ_v are the associated phases. The ωt term represents time evolution of the phase at frequency ω. For convenience, we normalize the intensity, setting $E_u^2 + E_v^2 = 1$. It is important to track individual phases rather than just the phase difference between components; while the difference is sufficient to describe the polarization state, the absolute phases are important for constructing a far-field diffraction pattern.

In order to determine the sense of rotation, we can look at the phase difference, $\delta \equiv \delta_v - \delta_u$. If we confine δ to the range $-\pi < \delta \le \pi$ by adding or subtracting integer multiples of 2π, we can associate $\delta < 0$ with right-hand polarization, and $\delta > 0$ with left-hand polarization, when adopting the convention of looking toward the light source. For instance, in Figure 2 the electric field vector will reach its maximum positive value in v (E_v) shortly before it reaches E_u. Therefore δ_u must be slightly less than δ_v in accordance with Eq. 5, so that $\delta > 0$ and we get left-handed polarization, as depicted. Linear polarization is described by $\delta = 0$ or $\delta = \pi$.

In order to transform the properties of the ellipse through a rotation by angle α, as defined

in Eq. 4 and depicted in Figure 2, we rotate an arbitrary electric field vector positioned somewhere on the ellipse by

$$\begin{pmatrix} E_s \cos(\omega t + \delta_s) \\ E_p \cos(\omega t + \delta_p) \end{pmatrix} = \begin{pmatrix} \cos\alpha & \sin\alpha \\ -\sin\alpha & \cos\alpha \end{pmatrix} \begin{pmatrix} E_u \cos(\omega t + \delta_u) \\ E_v \cos(\omega t + \delta_v) \end{pmatrix}. \tag{6}$$

We then separately equate all $\cos\omega t$ and $\sin\omega t$ terms in a trigonometric expansion of the terms above to find that

$$\begin{aligned} E_s \cos\delta_s &= E_u \cos\delta_u \cos\alpha + E_v \cos\delta_v \sin\alpha \\ E_s \sin\delta_s &= E_u \sin\delta_u \cos\alpha + E_v \sin\delta_v \sin\alpha \\ E_p \cos\delta_p &= E_v \cos\delta_v \cos\alpha - E_u \cos\delta_u \sin\alpha \\ E_p \sin\delta_p &= E_v \sin\delta_v \cos\alpha - E_u \sin\delta_u \sin\alpha \end{aligned} . \tag{7}$$

From this, one may compute the new phases via

$$\begin{aligned} \delta_s &= \mathrm{atan2}(E_s \sin\delta_s,\ E_s \cos\delta_s) \\ \delta_p &= \mathrm{atan2}(E_p \sin\delta_p,\ E_p \cos\delta_p) \end{aligned} , \tag{8}$$

which is insensitive to the values of E_s and E_p because these factors are common to the numerator and denominator of the arctangent argument. E_s and E_p can then be extracted by combining the results for δ_s and δ_p with Eq. 7. One may verify that $E_s^2 + E_p^2 = E_u^2 + E_v^2$ as a check on the computation.

At the front surface refractive interface, we diminish E_s and E_p according to the Fresnel equations—about 3.5% for fused silica at normal incidence—with s-polarization reflection increasing for larger incidence angles while p-polarization reflection decreases. Anti-reflection coatings would modify this procedure.

At each reflective interface within the CCR, the values of E_s and E_p will be preserved—either in TIR or for a perfect reflector. The phases, however, will shift according to the Fresnel relations for TIR:

$$\begin{aligned} \delta_s &\to \delta_s + \Delta\delta_s \\ \delta_p &\to \delta_p + \Delta\delta_p \end{aligned} , \tag{9}$$

where

$$\begin{aligned} \Delta\delta_s &= 2\tan^{-1}\left(\frac{\sqrt{n^2 \sin^2\theta - 1}}{n\cos\theta}\right) \\ \Delta\delta_p &= 2\tan^{-1}\left(\frac{n\sqrt{n^2 \sin^2\theta - 1}}{\cos\theta}\right) \end{aligned} , \tag{10}$$

with n being the refractive index of the medium (assuming vacuum on the other side) and θ being the angle of incidence determined by $\cos\theta = \left|\hat{\mathbf{k}} \cdot \hat{\mathbf{n}}\right|$. At normal incidence, each reflection has $\cos\theta = \frac{1}{\sqrt{3}}$ ($\theta \approx 54.74°$), so that fused silica at $n \approx 1.46$ results in $\Delta\delta_s \approx 1.31$ rad, and $\Delta\delta_p \approx 2.05$ rad. Our choice of conventions (e.g., Eq. 5) demands positive signs for Eq. 10 to match experimental results both in terms of polarization ellipses and diffraction pattern

8

orientations. For testing purposes, it is often useful to model perfect reflection, in which case δ_p is unchanged, while δ_s changes by π at each interface. In this case, the orientation and elliptical aspect of any polarization state is preserved in the global coordinate system on completing passage through the CCR, while the rotational sense switches handedness.

We therefore have a complete description of the procedure for tracking the four polarization parameters through the corner cube. On approach to each surface, the rotation angle of the current coordinate frame relative to the upcoming s–p frame is found; the polarization parameters are rotated into this frame; the phases are updated; the outbound $\hat{\mathbf{k}}$ and $\hat{\mathbf{p}}$ vectors are established; and the procedure repeats. Example code that can replicate all the results in this paper can be found at `http://physics.ucsd.edu/~tmurphy/papers/ccr-sim/ccr-sim.html`.

3.A. Matrix Approach

For normal incidence, we can cast the procedure into a Jones matrix approach:

$$\mathbf{T} = \mathbf{F} \cdot \mathbf{R}(\alpha_4) \cdot \mathbf{P} \cdot \mathbf{R}(\alpha_3) \cdot \mathbf{P} \cdot \mathbf{R}(\alpha_2) \cdot \mathbf{P} \cdot \mathbf{R}(\alpha_1), \tag{11}$$

where the rotation matrices, $\mathbf{R}$, use the angles provided in Table 1 according to

$$\mathbf{R}(\alpha) = \begin{pmatrix} \cos\alpha & \sin\alpha \\ -\sin\alpha & \cos\alpha \end{pmatrix}. \tag{12}$$

The Jones matrix, $\mathbf{P}$, is a diagonal matrix for advancing the phase of δ_s and δ_p:

$$\mathbf{P} = \begin{pmatrix} e^{i\Delta\delta_s} & 0 \\ 0 & e^{i\Delta\delta_p} \end{pmatrix}, \tag{13}$$

where the phase shifts are given by Eq. 10. Finally, in keeping with our approach in this paper of representing output states in the global coordinate frame, while the propagation direction has turned 180°, we apply a coordinate reflection,

$$\mathbf{F} = \begin{pmatrix} -1 & 0 \\ 0 & 1 \end{pmatrix}, \tag{14}$$

to the result. We have left out the reflection loss from the front surface to simplify the presentation.

For example, the composite matrix for the ACB path is

$$\mathbf{T}_{\mathrm{ACB}} = \begin{pmatrix} 0.655e^{2.78i} & 0.755e^{2.24i} \\ 0.755e^{1.51i} & 0.655e^{-2.16i} \end{pmatrix}. \tag{15}$$

We apply this matrix to an input polarization vector similar to that in Eq. 5. For instance we can describe a linear polarization input by the vector $\mathbf{P}_{\mathrm{in}} = \langle \cos\theta, \ \sin\theta \rangle$, where $\theta = 0$

represents polarization along the global x-axis. Circular polarization would have the vector $\mathbf{P}_{\text{in}} = \langle 1, \pm i \rangle / \sqrt{2}$. We then form the output polarization vector: $\mathbf{P}_{\text{out}} = \mathbf{T}\mathbf{P}_{\text{in}}$. For example, if $\theta = 45°$, we find that the ACB path produces $\mathbf{P}_{\text{out}} = \langle 0.962e^{2.49i}, 0.272e^{2.56i} \rangle$. Given the amplitudes P_x and P_y and the phase difference $\delta = \delta_y - \delta_x \approx 0.07$ in this case, we can find the polarization ellipse parameters by first constructing

$$\tan 2\omega t = -\frac{P_y^2 \sin 2\delta}{P_x^2 + P_y^2 \cos 2\delta}, \tag{16}$$

solving for ωt, then producing the ellipse vertices by:

$$\begin{aligned} x_1 &= P_x \cos \omega t \\ y_1 &= P_y \cos(\omega t + \delta) \\ x_2 &= P_x \cos(\omega t + \tfrac{\pi}{2}) \\ y_2 &= P_y \cos(\omega t + \tfrac{\pi}{2} + \delta) \end{aligned}, \tag{17}$$

after which one computes the semi-major and semi-minor axes via the Pythagorean distances from the origin created by coordinate pairs (x_1, y_1) and (x_2, y_2). The angle from the x-axis is then calculated as $\psi = \arctan(y/x)$ for the coordinate pair associated with the major axis. In the example case of 45° linear polarization following path ACB, we find that $a = 0.9998$, $b = 0.019$, and $\psi = 15.8°$. The state is nearly linear, and can be picked out in the fourth panel of Figure 3.

One must take care in interpreting the rotational sense of $\mathbf{P}_{\text{out}}$, because the coordinate flip matrix, $\mathbf{F}$, amounts to a reversal of $\hat{\mathbf{k}}$ relative to the s–p frame, reversing the association between the sign of δ and handedness. In this example case, with $\delta \approx 0.07$, the state is right-handed. Presenting polarization states in a global frame when $\hat{\mathbf{k}}$ turns 180° inevitably invites complication of this sort.

4. Polarization Results

Figure 3 shows the output polarization states computed for a fused silica CCR at normal incidence with a refractive index of around 1.46. After 60° degrees of rotation, the pattern repeats, albeit with an additional 180° rotation. Therefore, a 120° rotation results in an exact replication of the pattern with respect to the corner cube, in accord with the three-fold symmetry of the CCR. Tracking the output of a particular wedge reveals a smooth stepwise progression through ellipse eccentricity and rotation sense. Within each wedge, the orientation of the major axis tends to rotate slowly in a direction counter to the stepwise evolution of the input polarization angle.

For circular input polarization at normal incidence, there is no need to explore orientation changes. Figure 4 shows the rather symmetric polarization output patterns given circular input polarization into fused silica. For fused silica, the minor-to-major axis ratio is 0.168,
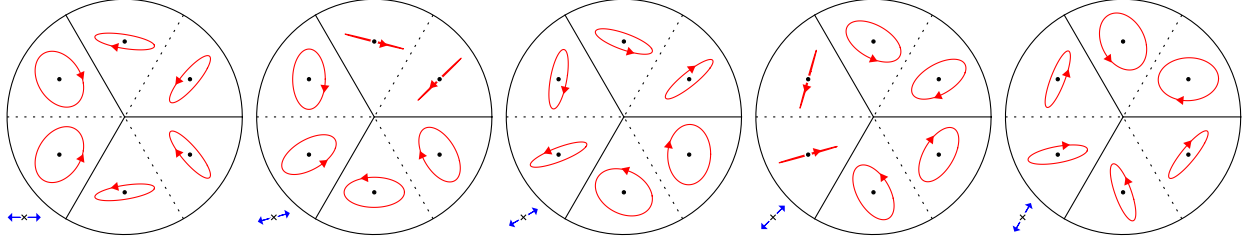
Fig. 3. Output polarization states at normal incidence for linear input polarization rotated in 15° increments. The input polarization is depicted at lower left, with a cross to indicate light traveling into the page. The output polarization is drawn in the wedge from which it emerges, as it would be oriented in the frame looking at the CCR face. Light output emerges from the page in this view (indicated by the dot in the center of each ellipse), so that right-handed polarization states show clockwise rotation. The pattern in the rightmost frame matches that in the leftmost frame with a 120° rotation.

while for BK7 it is 0.121. The output ellipses emerge with the same polarization sense as the input, although the arrows in the figure appear to be reversed on account of the reversal of light propagation direction.

As a computational check, Table 2 provides a sample of amplitudes and phases in the global x–y frame for normal incidence light polarized along the x-direction, leaving out the front-surface reflection loss. This corresponds to the left-most panel in Figure 3. We use a refractive index of 1.45702, corresponding to fused silica at 632.8 nm. Lurking in the δ_y column are phase pairs differing by π. Being at normal incidence, these results can be reproduced via the matrix method of Eq. 11, and the first row of the table is represented by the example matrix in Eq. 15.

4.A.   Experimental Comparison

Using a fused silica CCR and a HeNe laser at 632.8 nm, we directed a high-purity (10^5:1 intensity ratio) linear polarization state into each path sequence in turn, characterizing the emerging elliptical polarization state in terms of major and minor axes (taking the square root of measured intensity to find electric field amplitude), angle of the axis, and rotation sense with the help of a high-precision quarter-wave plate. The quarter-wave plate also provided an independent check of the ellipse axis ratio—this time directly as an electric field ratio. We employed a separate precision quarter-wave plate to send circular polarization into the CCR, confirming an axis ratio of 0.99 in amplitude. Figure 5 shows the results for two
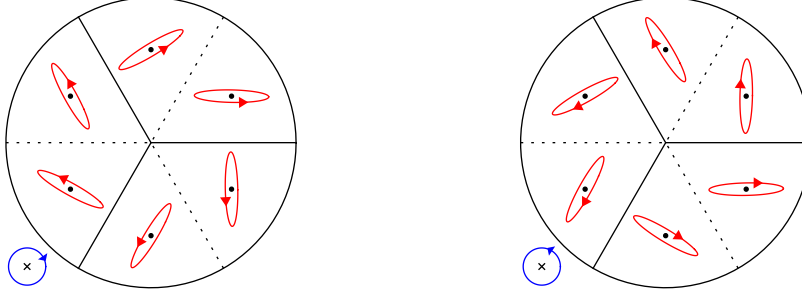
Fig. 4. Output polarization states at normal incidence for circular input polarization. Parameters and conventions are as described for Figure 3. The input light is depicted traveling into the page, so that left-handed polarization is seen at left, and right-handed at right.

Table 2. Example Electric Field Parameters[a]

Path	E_x	δ_x	E_y	δ_y
ACB	0.65547	2.77848	0.75523	1.51218
ABC	0.96282	−1.82634	0.27014	−2.83442
BAC	0.65547	2.77848	0.75523	−0.89783
BCA	0.65547	2.77848	0.75523	2.24376
CBA	0.96282	−1.82634	0.27014	0.30718
CAB	0.65547	2.77848	0.75523	−1.62941

[a]For normal incidence, horizontal input polarization

cases, in a format similar to that of previous plots.

We found in practice that the measured ellipse properties deviated more than we expected, given the purity of input polarization (see, for instance, the minor axis variations for the circular polarization case in Figure 5). Anomalies did not follow the CCR upon a 120° rotation of the CCR with respect to the optical bench, but stayed fixed in the laboratory frame, suggesting that the discrepancy resides in the measurement setup. The orientation of the major axis tends to be robust (within 10°), as this is a result of gross rotations (projections) of the input electric field vectors—both of which are controlled or known to adequate precision. The axis ratio, however, is very sensitive to phase differences between orthogonal polarizations, and could vary substantially. For the circular polarization case in Figure 5, the minor axis amplitude varies from 0.16 to 0.34 (expecting 0.17), while the
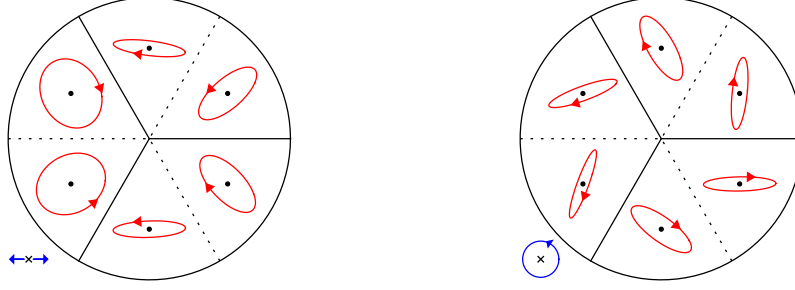
Fig. 5. Experimental polarization results, plotted following conventions in Figures 3 and 4. At left is linear polarization matching the left-most panel in Figure 3, and at right is right-handed polarization input. Slight irregularities are discussed in the text, but the overall agreement with theoretical expectations is good.

corresponding phase differences (δ, evaluated in a frame where the major axis has $\psi = 45°$) remain within 20° of theoretical expectations. For the linear polarization case, phase differences stayed within 15° of the expected values. Given the high degree of fidelity we observe in the far-field diffraction patterns—as demonstrated below—we conclude that the polarization states are indeed following the model closely, even if the results in Figure 5 do not appear to be an exact match.

5. Diffraction Method

The far-field diffraction pattern can be conveniently calculated via the Fourier transform (FT) of the complex amplitude and phase of the electric field at the exit aperture of the corner cube. The FT integrates area-weighted amplitude and phase contributions at the aperture, resulting in the net sum—or interference—of the electric field at infinite distance as a function of angular displacement from the propagation direction. The square magnitude of the FT then represents the intensity in the far-field:

$$I(\chi, \eta) = \left| \int \int_{\text{aperture}} S(u, v) \exp\left[i\phi(u, v)\right] \exp\left[ik(\chi u + \eta v)\right] \mathrm{d}u \mathrm{d}v \right|^2, \qquad (18)$$

where the aperture amplitude, S, and phase, ϕ, are functions of coordinates u and v in the aperture plane. The coordinates χ and η then represent angular coordinates in the far-field, with $k = 2\pi/\lambda$.

Orthogonal polarizations cannot interfere with each other, so the Fourier transform must be broken into separate computations for any two orthogonal polarizations. For each, the phases are simply the final δ_u and δ_v phases resulting from the transformation of the final

values of δ_s and δ_p computed via sequential applications of Eq. 10 into some final u–v coordinate frame. Each wedge in the aperture—corresponding to each of the six unique path sequences—will have constant phase across the wedge.

The aperture function can be determined during preparation for the Fourier transform, in that one must pass to the integral a two-dimensional array of aperture amplitudes in the input u–v frame. By raytracing a grid of input ray positions sharing the same input $\hat{\mathbf{k}}$ vector, one can determine which rays emerge by rejecting any ray that encounters any of the four CCR planes outside the cylindrical radius of the CCR. The resulting aperture for non-normal incidence has a shape given by the included intersection of two equal ellipses shifted relative to one another along their minor axes, each one representing the projected rim of the entrance aperture and the retro-reflected rendition of the same. The raytrace also determines which sequence (wedge) applies, and thus which amplitudes among the set of six pre-computed E_u and E_v values are to be used for $S(u,v)$.

One can readily compute the central irradiance, $I(0,0)$, of the far-field diffraction pattern in the normal incidence case simply by summing the aperture function, $S(u,v)$, times the phase function, $\exp\left[i\phi(u,v)\right]$, equally weighted for all six wedges. In the trivial case where $S = 1$ inside a circular aperture of radius R while ϕ is constant, we get a central irradiance of $\pi^2 R^4$. Summing the values in Table 2 (where $E \to S$ and $\delta \to \phi$), each weighted by $\pi R^2/6$, we get a central irradiance for the x-component of:

$$I(0,0) = \left| \frac{\pi R^2}{6} \sum_{n=1}^{6} S_n e^{i\phi_n} \right|^2 \approx 0.264\pi^2 R^4, \tag{19}$$

and a y-component summing to zero. Thus the total central irradiance of the TIR diffraction pattern is 26.4% of what it would be for a perfect Airy pattern. Combining this with reflection loss from an uncoated fused silica front surface (incurred twice) puts the central irradiance at 24.6% that of the Airy pattern for a circular aperture of the same diameter.

We can develop a useful tool for computing the expected central irradiance in the far-field diffraction pattern if we characterize all the flux as being contained in a tophat pattern whose uniform intensity is set to that of the central peak of the actual diffraction pattern. This crude model permits a simple estimation of the central intensity, once the tophat diameter is known. Expressed in terms of the diffraction scale, an uncoated fused silica CCR is characterized by a tophat diameter of $2.56\lambda/D$. For the Apollo corner cubes at 532 nm, this is 7.4 arcsec. The corresponding measure for a perfect Airy pattern is $1.27\lambda/D$. Conversely, if we conveniently—albeit naïvely—modeled the diffraction pattern as containing all the flux within a tophat diameter set to λ/D, we find that the central irradiance of the actual pattern is reduced to 0.152 times the nominal value suggested by the simple λ/D tophat model. Reflection losses at the front surface degrade the performance further.

14

6.   Far-field Diffraction Results

In the diffraction patterns we present, the orientation convention is in keeping with those in the rest of the paper: looking at the corner cube. Thus the global $+\hat{\mathbf{x}}$ direction is to the right, and $+\hat{\mathbf{y}}$ is up. Direction cosines are plotted, so that light arriving at positive-x global coordinates in the far field are shown to the right. If projected onto a screen at infinity, each of the images here would incur a left-right flip. The horizontal direction follows that used to define polarization, being perpendicular to the plane of incidence and therefore lying in the global x–y plane.

At normal incidence, the azimuthal orientation of the input polarization impacts the output polarization state, as seen in Figure 3. Following the same CCR rotation sequence and input polarization as was used in Figure 3, we produce the far-field diffraction patterns in Figure 6. The polarization state of the central peak follows that of the input polarization. The total diffraction pattern rotates by 120° as the polarization rotates through 60° in the opposite direction, producing a net 180° rotation of the pattern with respect to the polarization state—just as the polarization ellipses did in Figure 3.

Figure 7 shows two profiles through the normal incidence TIR CCR diffraction pattern compared to the scaled Airy pattern. The two profiles correspond to orthogonal cuts through the center of the pattern in the upper-left panel of Figure 6, one of which passes through two outer lobes, and the other passing between lobes. The plot shows the symmetry of the central peak, and its similarity to the Airy function over a considerable radius. In units of λ/D, the TIR pattern departs from the Airy pattern by 1% of full scale at a radius of 0.30, by 5% at 0.47–0.48, and by 10% at 0.59–0.61, where ranges refer to the two different profiles. The functional form away from the central peak is particularly relevant for satellite and lunar ranging applications, where the tangential velocity of the target results in a shift (velocity aberration) of the diffraction pattern at the position of the transmitter, so that a co-located receiver samples the shoulder of the diffraction pattern rather than its peak. Lunar ranging to the 38 mm diameter CCRs at 532 nm imposes a velocity aberration of 4–6 μrad, which corresponds to about 0.29–0.43 λ/D. The Airy function is therefore still accurate to within 5% in this regime, for normal incidence.

As we move away from normal incidence, we may consider the effect of azimuth and inclination angle on the patterns. We present results in a 4×4 grid corresponding to off-axis positions on a 5° pitch and in a Pythagorean arrangement. We place the normal incidence case at the upper left, so that the fourth panel over in the top row corresponds to an inclination angle of 15° and an azimuth of $A = 0°$, as defined in Section 2. This corresponds to the distant observer placed in the positive-x direction in the global coordinate frame of Figure 1, with $y = 0$. The second panel over in the bottom row has an inclination angle of $\sqrt{15^2 + 5^2} \approx 15.8°$ and an azimuth of $\arctan(-15/5) \approx -72°$, putting the observer at a
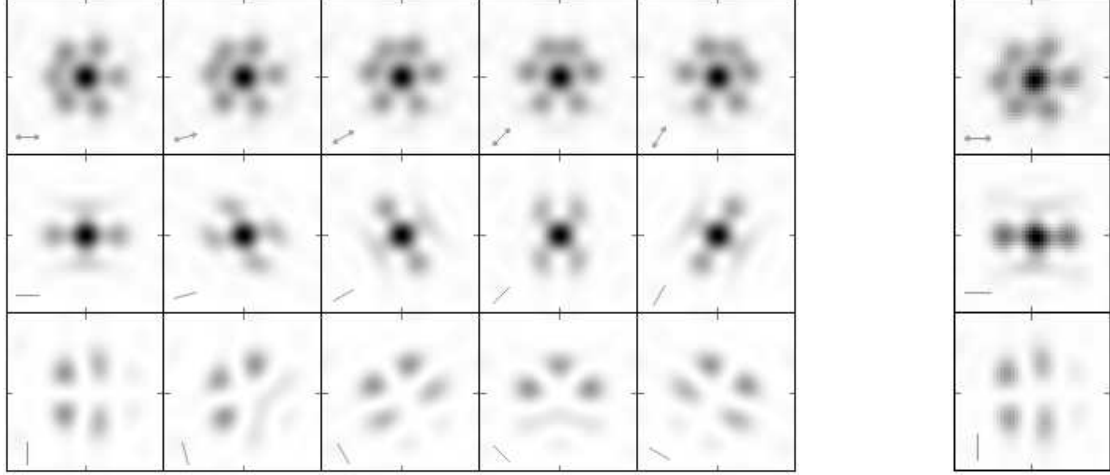
15

Fig. 6. Normal incidence far-field diffraction patterns for five orientations of linear polarization input in 15° increments, paralleling the sequence in Figure 3. The top row is total irradiance, indicating input polarization direction in the lower-left corner of each panel; the middle row is the polarization component parallel to the input polarization (indicated lower left in each panel); the bottom row is the orthogonal polarization component (also indicated lower left in each panel). At right is the experimental result corresponding to the first column in the set of model results at left. Each frame is $50\lambda/7D$ radians across. Intensities are normalized to the same value in all frames.
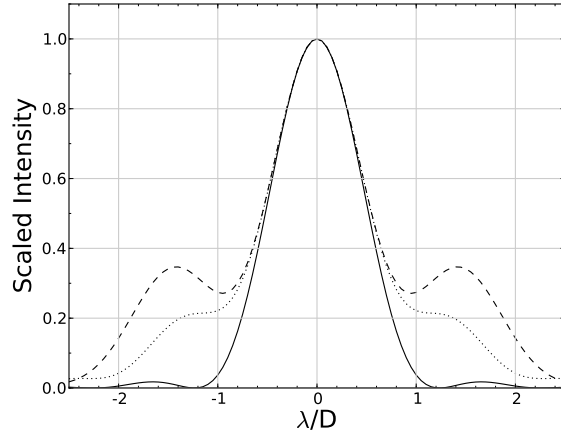
Fig. 7. Orthogonal cuts (dashed and dotted) through the normal incidence far-field diffraction pattern for the TIR CCR under linear input polarization, showing the similarity of the central peak to the scaled Airy function (solid). The cuts correspond to the upper left panel of Figure 6.

positive-x coordinate, with $y = -3x$. Figure 8 shows the appearance of the effective apertures as seen by the observer in these positions.

For horizontal polarization input—which we define as perpendicular to the plane of incidence—we get the patterns seen in Figure 9. For vertical input polarization, the patterns look the same, but with a 180° rotation of all frames and the middle panel corresponding to vertical polarization output and the rightmost panel corresponding to horizontal output.

The far-field diffraction patterns for left-handed circular input polarization are shown in Figure 10. The patterns for right-handed circular polarization are the same except for a 180° rotation of each frame and an exchange of horizontal and vertical polarizations. The normal-incidence pattern has a three-fold symmetry lacking in the linear polarization case, which stems from the complete orientation-invariance of circular polarization, so that only the corner cube asymmetries may imprint on the diffraction pattern. Evidence for symmetry is also clear in the polarization patterns of Figure 4.

6.A.   *Laboratory Results*

We formed a linearly-polarized plane wave from a HeNe laser across a 25 mm diameter, having a wavefront quality of approximately $\lambda/4$ as judged visually by a shear plate. To achieve a uniform spatial intensity across the aperture, we placed a $D = 9.1$ mm circular aperture in front of the CCR, concentric with and close to the front face (wavefront quality
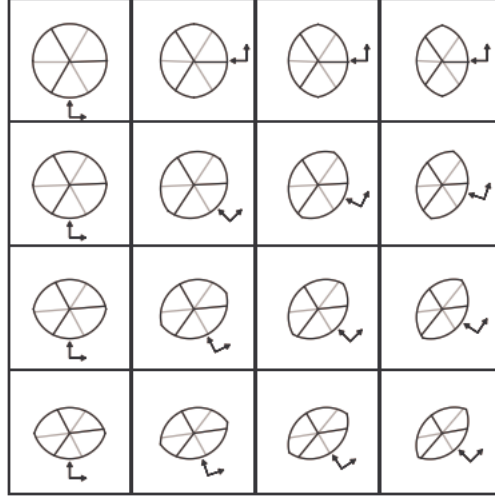
17

Fig. 8. Orientation scheme and aperture shapes for the diffraction patterns to follow. Normal incidence is at upper left, with each tile representing a 5° step along the positive-x axis to the right and along the negative-y axis in the down direction. The horizontal-vertical basis vectors ($\hat{\mathbf{s}}_0$ and $\hat{\mathbf{p}}_0$) are placed at the azimuthal position of the observer, vertical pointing toward the aperture. Black lines represent the refracted appearance of real edges, while gray lines are the reflected edges.
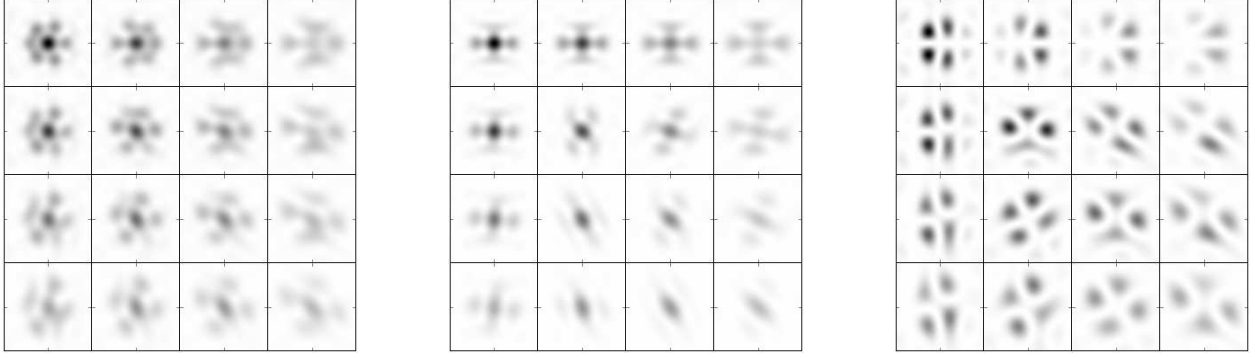
Fig. 9. Diffraction patterns for horizontal linear input polarization at a range of viewing angles. In each grid, the upper left panel is at normal incidence, following the orientation scheme depicted in Figure 8. At left is the total intensity, followed by the horizontal and vertical polarization components. Intensities are normalized to a common maximum within each of the three sets, but the intensity of the vertical polarization panel has been scaled by a factor of 2.57 relative to the other two in order to show details in these intrinsically dimmer patterns.
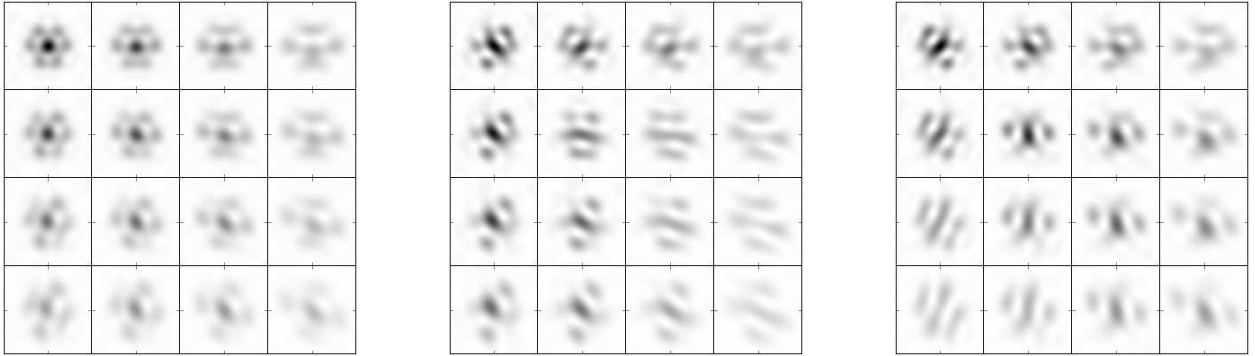

Fig. 10. Diffraction patterns for left-handed circular input polarization, following the conventions of Figures 8 and 9. The horizontal and vertical polarization decomposition does not in this case break cleanly into distinct patterns as was the case for linear input polarization, since the central spot in this case is circularly polarized and thus shares equally in the two components.
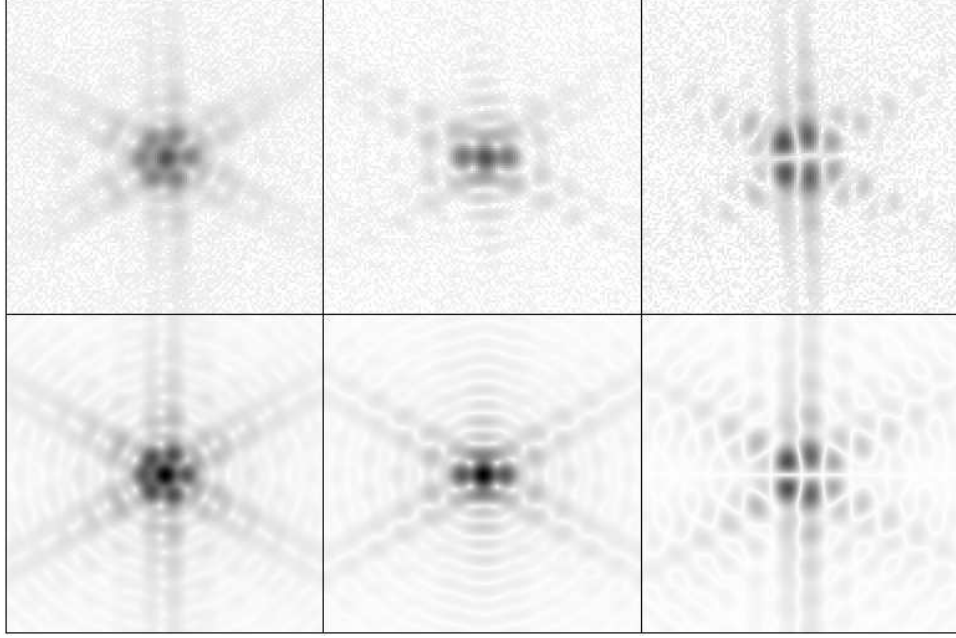
19

Fig. 11. Comparison of experimental results (top) to the simulation results (bottom), stretched to emphasize faint structure. At left is total intensity given horizontal polarization input light, followed by horizontal and vertical polarization output patterns. Each frame is $64\lambda/3D$ across.

was better over the smaller aperture). The CCR used was a 25.4 mm diameter high-precision fused silica corner cube. We also tested a flight spare CCR from the Apollo retroreflector arrays, finding similar results—albeit with increased scattered light and diffraction spikes owing to the intentionally–ground edges where the rear CCR surfaces meet occupying a significant fraction of the 9 mm aperture.

The beam passed through an uncoated fused silica wedge window having $\lambda/10$ surface quality before striking the CCR at normal incidence. The wedge window was tilted to reflect the returning beam away from the optical axis by an angle of approximately 10° for access to imaging. A 339 mm focal length lens produced a far-field pattern onto a CCD camera with 3.65 μm pixels. This results in 15.75 pixels spanning the $2.44\lambda/D$ Airy diameter. Replacing the corner cube with a flat mirror produced an Airy pattern having azimuthally uniform rings and approximately 84% of the total flux within the first dark ring, as expected. The same measure performed on the TIR pattern under horizontal polarization produced $36.1 \pm 0.6\%$, in perfect agreement with the theoretical expectation.

The experimental diffraction pattern images in Figure 11 have been rotated and reflected to

place the experimental results in the same frame established for the simulated patterns (i.e., transformations followed the physical setup, and are not simply forced to match simulations).

7.   Conclusions

The polarization states and resulting diffraction patterns from TIR CCRs are non-trivial and generally require computational tools to assess. This paper presents a comprehensive methodology for doing so, and provides results against which independent analyses may be compared. The results compare well against some—but not all—items available in the literature, and laboratory measurements confirm the validity of the mathematical development. The Python code that generated all simulation results contained in this paper is available at `http://physics.ucsd.edu/~tmurphy/papers/ccr-sim/ccr-sim.html`.

This tool can provide a springboard from which one might analyze aberrations from manufacturing imperfections, intentional offset angles of the rear surfaces, thermally-induced refractive index gradients, aperture masking or blockage, non-planar wavefront input, etc. In a companion paper [10], we explore the impact of thermal gradients on the diffraction patterns from TIR corner cube prisms.

References

1. E. R. Peck, "Polarization Properties of Corner Reflectors and Cavities," J. Opt. Soc. Am. **52**, 253–258 (1962).
2. J. Liu, and R. M. A. Azzam, "Polarization properties of corner-cube retroreflectors: theory and experiment," Appl. Opt. **36**, 1553–1559 (1997).
3. R. R. Hodgson, and R. A. Chipman, "Measurement of corner cube polarization," SPIE Polarimetry **1317**, 436–447 (1990).
4. M. S. Scholl, "Ray trace through a corner-cube retroreflector with complex reflection coefficients," J. Opt. Soc. Am. A **12**, 1589–1592 (1995).
5. R. F. Chang, D. G. Currie, C. O. Alley, and M. E. Pittman "Far-Field Diffraction Pattern for Corner Reflectors with Complex Reflection Coefficients," J. Opt. Soc. Am. **61**, 431–438 (1971).

6. D. A. Arnold, "Method of calculating retroreflector-array transfer functions," Smithsonian Astrophysical Observatory Special Report **382**, (1979).

7. M. A. Sadovnikov, and A. L. Sokolov, "Spatial Polarization Structure of Radiation Formed by a Retroreflector with Nonmetallized Faces," Opt. Spektrosk. **107**, 213–218 (2009).

8. A. L. Sokolov, and V. V. Murashkin, "Diffraction Polarization Optical Elements with Radial Symmetry," Opt. Spektrosk. **111**, 900–907 (2011).

9. T. W. Murphy, Jr., E. G. Adelberger, J. B. R. Battat, L. N. Carey, C. D. Hoyle, P. LeBlanc, E. L. Michelsen, K. Nordtvedt, A. E. Orin, J. D. Strasburg, C. W. Stubbs, H. E. Swanson, and E. Williams, "The Apache Point Observatory Lunar Laser-ranging Operation: Instrument Description and First Detections," Publications of the Astronomical Society of the Pacific **120**, 20–37 (2008) (`http://arXiv:0710.0890`).

10. S. D. Goodrow, and T. W. Murphy, Jr., "Effects of thermal gradients in total internal reflection corner cubes," Appl. Opt. **51**, 8793–8799, (2012).

11. T. W. Murphy, Jr., E. G. Adelberger, J. B. R. Battat, C. D. Hoyle, R. J. McMillan, E. L. Michelsen, R. L. Samad, C. W. Stubbs, and H. E. Swanson, "Long-term degradation of optical devices on the Moon," Icarus **208**, 31–35 (2010) (`http://arXiv:1003.0713`).